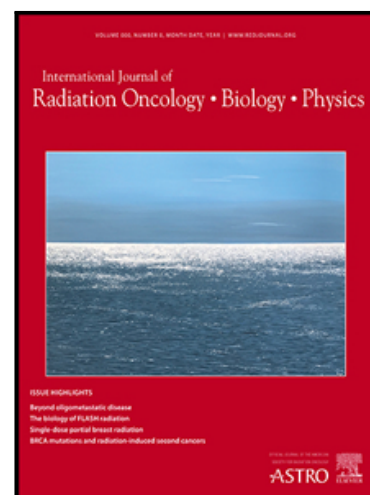# Journal Pre-proof

Microbeam Radiation Therapy controls local growth of radioresistant melanoma and treats out-of-field locoregional metastasis

Verdiana Trappetti PhD , Marine Potez PhD ,
Cristian Fernandez-Palomo PhD , Vladislav Volarevic ,
Nahoko Shintani PhD , Paolo Pellicioli PhD , Alexander Ernst PhD ,
David Haberthür PhD , Jennifer M. Fazzari PhD ,
Michael Krisch PhD , Jean A. Laissue MD ,
Robin L. Anderson PhD , Olga A. Martin PhD ,
Valentin G. Djonov MD

Please cite this article as: Verdiana Trappetti PhD , Marine Potez PhD , Cristian Fernandez-Palomo PhD , Vladislav Volarevic , Nahoko Shintani PhD , Paolo Pellicioli PhD , Alexander Ernst PhD , David Haberthür PhD , Jennifer M. Fazzari PhD , Michael Krisch PhD , Jean A. Laissue MD , Robin L. Anderson PhD , Olga A. Martin PhD , Valentin G. Djonov MD , Microbeam Radiation Therapy controls local growth of radioresistant melanoma and treats out-of-field locoregional metastasis, *International Journal of Radiation Oncology, Biology, Physics* (2022), doi: https://doi.org/10.1016/j.ijrobp.2022.06.090

Title: Microbeam Radiation Therapy controls local growth of radioresistant melanoma and treats out-of-field locoregional metastasis

Short Running Title: MRT treats melanoma and metastasis

Author Names: Verdiana Trappetti PhD[1&], Marine Potez PhD[1,2&], Cristian Fernandez-Palomo PhD[1], Vladislav Volarevic[1,3], Nahoko Shintani PhD[1], Paolo Pellicioli PhD[4], Alexander Ernst PhD[1], David Haberthür PhD[1], Jennifer M. Fazzari PhD[1], Michael Krisch PhD[4], Jean A. Laissue MD[1], Robin L. Anderson PhD[5,6], Olga A. Martin PhD[1,7,8%*], Valentin G. Djonov MD[1%*]

Author Institutions:
[1] Institute of Anatomy, University of Bern, Baltzerstrasse 2, 3012 Bern, Switzerland;
[2] Department of Neuro-Oncology, H. Lee Moffitt Cancer Center and Research Institute, 12902 USF Magnolia Drive, 33612 Tampa, FL, USA;
[3] Center for Molecular Medicine and Stem Cell Research, Department of Microbiology and immunology, Faculty of Medical Sciences, University of Kragujevac, Jovana Cvijića 6б, 34000 Kragujevac, Serbia;
[4] Biomedical Beamline ID17, ESRF, The European Synchrotron, 71 Avenue des Martyrs, CS40220, 38043 Grenoble Cedex 9, France
[5] Olivia Newton-John Cancer Research Institute, 145 Studley Rd, Heidelberg, VIC, 3084, Australia;
[6] School of Cancer Medicine, La Trobe University, Plenty Rd &, Kingsbury Dr, Bundoora, VIC, 3086, Australia;
[7] Division of Radiation Oncology, Peter MacCallum Cancer Centre, 305 Grattan St, 3000 Melbourne, VIC, Australia;
[8] University of Melbourne, Parkville, VIC, 3010, Australia.

[&] Equal contribution of VT and MP
[%] Equal contribution of OAM and VGD

Corresponding authors[*]: Dr Olga Martin & Dr Valentin Djonov. Address: Institute of Anatomy, University of Bern, Bern, Switzerland; Baltzerstrasse 2, 3012 Bern, Switzerland. Emails: olga.martin@unibe.ch; valentin.djonov@unibe.ch

Author Responsible for Statistical Analysis: Valentin Djonov, valentin.djonov@unibe.ch

Conflict of interest statement: The authors declare no potential conflicts of interest.

1

Abstract

Purpose

Synchrotron-generated microbeam radiotherapy (MRT) represents an innovative preclinical type of cancer radiotherapy with an excellent therapeutic ratio. Beyond local control, metastatic spread is another important endpoint to assess the effectiveness of radiotherapy treatment. Currently, no data exists on an association between MRT and metastasis. Here, we evaluated the ability of MRT to delay B16F10 murine melanoma progression and locoregional metastatic spread.

Methods and Materials

We assessed the primary tumor response and the extent of metastasis in sentinel lymph nodes in two cohorts of C57BL/6J mice, one receiving a single MRT and another receiving two MRT delivered with a 10-day interval. We compared these two cohorts with synchrotron broad beam-irradiated and non-irradiated mice. In addition, using multi-plex quantitative platforms, we measured plasma concentrations of 34 pro- and anti-inflammatory cytokines and frequencies of immune cell subsets infiltrating primary tumors that received either one or two MRT treatments.

Results

Two MRT treatments were significantly more effective for local control than single MRT. Remarkably, the second MRT also triggered a pronounced regression of out-of-radiation field locoregional metastasis. Augmentation of CXCL5, CXCL12 and CCL22 levels after the second MRT indicated that inhibition of melanoma progression could be associated with increased activity of anti-tumor neutrophils and T-cells. Indeed, we demonstrated elevated infiltration of neutrophils and activated T-cells in the tumors following the second MRT.

Conclusions

Our study highlights the importance of monitoring metastasis following MRT and provides the first MRT fractionation schedule that promotes local and locoregional control with the potential to manage distant metastasis.

Introduction

Recent advancements in radiotherapy (RT) technology have contributed to the improved therapeutic ratio of radiation treatment, one of the most common modalities used to eradicate cancer. Historically, crude spatial fractionation of radiation was used to deliver ablative radiation doses that could achieve local control with minimal toxicity (1). A renewed interest in this concept led to the development of more sophisticated spatially fractionated RT (SFRT) modalities that further exploit its normal tissue sparing effect. The innovative concept of microbeam RT (MRT), a 'next-generation SFRT' produced by synchrotron sources, is a novel paradigm for radiation treatment bolstered by its remarkable preclinical results (2). In MRT, a collimator subdivides the homogeneous radiation field into planar beams of X-rays, delivered at exceptionally high dose rates, into µm-range, high dose areas ("peaks"), separated by a few hundred µm of low dose regions ("valleys"). Spatially segmented dose deposition drastically increases the maximum dose that can be delivered by each one of the microbeams triggering a cascade of biological responses that improve tumor control without inducing normal tissue toxicities (3,4).

Melanoma is the most aggressive and radioresistant form of skin cancer. Melanoma cell survival following RT has been historically attributed to efficient repair of radiation-induced DNA damage and corroborated by recent studies (5,6). Since RT alone is not able to completely eradicate melanoma, it is used as part of a palliative treatment strategy, when surgery cannot be performed, or as an adjuvant therapy following lymphadenectomy. Conventional irradiation of murine B16F10 melanomas with a single dose of 15 Gy slowed tumor progression only initially, while fractionated irradiation (3 Gy x 5) was not effective (7). It has been recently reported superior

4

tumor control following synchrotron MRT relative to broad beam (BB) irradiation, in the B16F10 melanoma model (8). A single 407.6 Gy peak-dose MRT lead to a pronounced impairment of tumor vascular perfusion, reduction of proliferation and induction of senescence in tumor cells and production of monocyte- and lymphocyte-attracting chemokines that resulted in increased accumulation of natural killer (NK) cells and cytotoxic T-lymphocytes (CTLs) to the tumors (8,9). In the same model, local control was significantly improved by substitution of a single MRT irradiation of 401.23 Gy peak dose with three daily administrated 133.41-Gy fractions (10). Such temporal fractionation with a cross-beam configuration completely ablated half of the tumors and significantly increased the median survival in the remaining animals, compared to the cohort irradiated with a single MRT.

As well as local control, locoregional and distant metastasis are important endpoints in assessing the effectiveness of RT treatment. Currently, no data exists on the potential impact of MRT on melanoma metastasis. Treatment of solid tumors is currently based on consideration of three clinical staging parameters affecting prognosis: the primary tumor size, tumor spread to proximal lymph nodes (LNs) and distant metastasis (11). Even after successful local treatment of primary malignancies, metastasis is common, and uncontrollable metastatic disease is generally the cause of cancer-related death (12). Post-RT metastases can arise from pre-existing subclinical micro-metastases (13). However, there is evidence from both animal and clinical studies, that conventional RT itself can increase the risk of tumor cell dissemination from solid tumors (14,15).

LN-positivity, especially growth of nodal metastasis into adjacent tissues, has been associated with an increased risk of recurrence and poor overall survival in patients with locally advanced cancers (16). For melanoma, regional LNs are a common site

of disease spread (17). Sentinel LN dissection, as well as adjuvant locoregional RT, is standard practice, since it is associated with improved distant metastasis-free survival and, in some clinical trials, with overall survival (18). Conversely, without evidence of metastatic LNs or distant metastasis, usually no further therapy is recommended, beyond treatment/excision of the primary lesion. All these management policies infer that the tumor cells in intra-nodal metastases are capable of further dissemination and infiltration of other organs, however, this assumption is a point of ongoing debate (19). An alternative hypothesis is that distant metastases can only be generated by cells disseminated from the primary tumor, and positive LNs are a surrogate for the biological propensity of the tumor to metastasize (19).

In this context, it is of extreme importance to understand the propensity of MRT to induce or modulate metastases and underlying radiobiological mechanisms, to provide a roadmap for further research on improving treatment outcomes. Here, we report the effectiveness of two fraction- *vs.* single fraction-MRT (2F *vs.* SF) not only by measuring the primary tumor volume, but also by assessing metastasis in locoregional sentinel LNs. To further support our findings, we assessed if the second MRT would modulate secretion of plasma cytokines and the local immune cell composition, to generate an anti-tumor immune response and enhance tumor regression following MRT, both locally and locoregionally.

Methods and Materials

Animals, tumor induction and follow-up. Animal experiments were performed under permit XXXX approved by the Veterinary Office of XXXX, and under the license number XXXX provided by the XXXX Internal Evaluation Committee for Animal Welfare and Rights. C57BL/6J mice (females, 8 weeks old, Charles River Laboratories, XXXX), were used. After induction of anesthesia (cocktail of fentanyl (0.05 mg/kg body weight [BW]), midazolam (5 mg/kg BW), and medetomidine (0.5 mg/kg BW)), 120,000 mycoplasma-free B16F10 melanoma cells (American Type Culture Collection, Manassas, VA, USA) were implanted in mouse ear pinnae by microsurgery (one tumor in each ear, two tumors per mouse), as previously described (20). Once the tumors were visible, starting from day 9 post-implantations, they were measured daily with an electronic caliper and tumor volume *V* was calculated with the following formula $V = \frac{4\pi}{3} * \frac{a}{2} * \frac{b}{2} * \frac{c}{2}$ (*a*, *b* and *c* are the length, width and thickness of the tumor) until the day of mouse euthanasia. Mice were culled with an IP injection of sodium pentobarbital (200 mg/kg BW), when ulceration on at least one of the tumors was detected.

Irradiations. BB and MRT were delivered with synchrotron X-rays at XXXX biomedical beamline, XXXX. For MRT, a polychromatic photon spectrum with an average energy of 104 keV and an average dose rate of 13 kGy/s was used. An XXXX multislit collimator designed with 50 μm wide apertures (21) was used to spatially define the thickness of the planar beams and the 200 μm center-to-enter spacing between them ('valleys'). For the first MRT the dose was 396.19 Gy for the peak and 6.56 Gy for the valley; for the second MRT, 396.06 Gy and 6.45 Gy, respectively. For BB irradiation, the homogenous dose delivered was 6.2 Gy which

nearly corresponds to the MRT valley dose. The scatter radiation dose received at the site of the mouse neck was in the range of 34-50 mGy.

Fourteen mice from the SF-MRT cohort were irradiated once on day 11 after tumor implantation (designated D0 in **Figure 1A**), and 20 mice from the 2F-MRT cohort received the second MRT dose on day 21 after tumor implantation (designated D10 in **Figure 1A**). The 10-day interval between the two MRT sessions was chosen because at D10 the tumor growth was at the nadir. The orientation of the beam relative to the mouse ears is depicted in Figure 1A. For the first MRT, the body of the mouse was aligned vertically and rotated so that pinna of the ear was approximately orthogonal to the microbeam planes, with the field (7.5-mm wide and 15.0-mm high) located centrally over the tumor (8). For the second MRT, mice were positioned horizontally which rotated the ears 90° from the first irradiation, so the tumors were irradiated in a crossed geometry, with a field size of 8.0×8.0 mm.

Analysis of LNs. Both the right and left largest superficial cervical lymph nodes (sentinel LNs) from melanoma-bearing mice were examined. LNs from earlier experiments with the B16F10 melanoma model were also analyzed. All the experiments involved the following settings: MRT 396 Gy peak dose at D0; MRT 396 Gy peak dose SF at D0 and 2F at D10; BB 6.2 Gy SF (approximately equivalent to the MRT valley dose) at D0, and non-irradiated controls. The paraformaldehyde (PFA)-fixed LNs were stored for up to 5 years for the earlier experiments. In most cases, both left and right sentinel LNs were harvested, from mice sampled at D2-D37 post-first irradiation. The animal ethics protocol mandated euthanasia of mice with ulcerated tumors, which for non-irradiated control mice occurred before 22 days post-

tumor implantation. Thus, LNs from control mice were harvested at one day prior-to-irradiation (D-1) and at D2-D11 post-SF-MRT.

LNs were fixed in a 4% PFA solution and examined macroscopically. The size of the LNs was measured and the volume occupied by metastases was estimated. The scoring system was adapted from our previous study (20).

Dosimetry, photography and microtomography of LNs, immunohistochemistry, microscopy, immune analysis of plasma samples and irradiated tumors are described in **Supplementary Materials**.

Statistical analysis. GraphPad Prism version 9 (GraphPad Software, San Diego, CA, USA) was used for data presentation and statistical analyses. The two-way ANOVA multiple comparison test was used to analyze differences in the tumor growth curves (SF-MRT *vs*. 2F-MRT). The one-way ANOVA multiple comparison test was employed to analyze differences in LN metastasis score over time. The Kruskal–Wallis non-parametric multiple comparison test was applied to analyze differences in LNs sizes within different weeks post-irradiation and in the cytokine time course. In both the LN score and size evaluation, one group (BB at week 4) had a very small sample size (only 4 LNs). We report the data in our plots, although no statically significance with such a small sample size could be underlined. The nonparametric Mann–Whitney test was used to analyze the differences between relative immune populations detected by the ChipCytometry assay.

Results

The second MRT elicits better tumor control

At D0, melanoma-bearing mice were assigned to two groups, 'SF-MRT' and '2F-MRT', to receive either one or two MRT treatments with 396-Gy peak dose and 6.5-Gy valley dose, with the expectation that administering the second radiation dose would further delay tumor progression. Indeed, as shown in **Figure 1B**, remarkably attenuated tumor progression was observed in 2F-MRT-treated melanoma-bearing mice compared to those animals that received only one MRT treatment. The mean tumor volume was significantly lower in the 2F-MRT cohort than in the SF-MRT cohort starting from D15 after the first MRT. In a retrospective analysis of the MRT treatment response of each melanoma in the two different MRT cohorts, the growth of the irradiated tumors was further sub-classified according to their response to MRT treatment. After the first MRT, two different types of tumor responses were identified: 85.7% of melanomas shrank, but subsequently regrew (SF Response), while 14.3% were virtually unresponsive, with no tumor shrinkage but had a slight delay in tumor growth with respect to the non-irradiated controls (SF Partial response) (**Figure 1C**). After the second MRT, three different types of tumor responses were registered: 25% of melanomas experienced complete remission (2F Complete response), 65% shrank but subsequently regrew (2F Response), and only 10% showed a slight delay of tumor growth with no tumor shrinkage (2F Partial response) (**Figure 1D**). BB irradiations, as previously reported (8), impaired tumor growth starting from D5 when compared to non-irradiated tumors, however, no tumor shrinkage was observed. This is significantly inferior to the tumor growth delay elicited by SF-MRT and 2F-MRT.

The second MRT significantly delays progression of locoregional metastasis

11

The black pigment melanin produced by melanoma cells, provided a unique means to visualize locoregional metastasis. The right and left cervical sentinel LNs were harvested per each mouse. We evaluated the proportion of positive sentinel LNs in the experimental cohorts and other clinically relevant factors, such as LN size and extent of LN metastasis. Over the years, we have accumulated a large collection of LNs from melanoma-bearing mice treated as presented in **Figure 1A** along with corresponding non-irradiated controls. For a comprehensive study of locoregional metastasis, the entire LN collection was analyzed. Partly, the examined LNs were from the current experiment, while the rest were from previous experiments (8,20) and yet unpublished experiments. It was determined that the scatter radiation dose received by LNs following irradiation of the ears was in the range of 34-50 mGy.

Fraction of positive LNs in experimental cohorts. On D2, macroscopic metastases were present in 7.1% of sampled LNs of non-irradiated melanoma-bearing mice, in 60% of LNs of SF-MRT-treated mice, and in 22.2% of LNs of BB-treated mice. The metastatic growth progressed rapidly; on D5 the respective values were 47.6%, 91.7% and 96.1%. In all cohorts, at later time-points (up to D37), metastases were observed in the vast majority of examined LNs (**Table S1**). Immunostaining of macroscopically negative sentinel LNs indicated that they can contain cells positive for melanoma markers Melan A and S-100β (**Figure S1**). Therefore, while locoregional metastasis is an expected consequence of primary tumor growth, both SF-MRT and BB irradiations accelerated this process compared to non-irradiated controls.

Size of LNs. The size of individual LNs as well as the median values in all experimental cohorts over time post-irradiation are shown in **Figure 2**. We pooled the data into weekly bins, since this presentation provided a reasonable cohort size for

comparison. The mean LN sizes were generally similar, mostly in the range of 2-5 mm (representative images are shown in **Figure 3A**). Four outliers in the SF-MRT 2-week group were underlined using the ROUT method with Q=1%, however we decided not to exclude these samples from analysis because of their clinical relevance. The significance was calculated employing median, rather than mean measures, to limit the contribution of the four samples to the final statistical significance. One of these four LNs harvested on D23 post-SF-MRT, was of 17.2 mm-size and completely invaded by melanoma cells (**Figure S1E**).

Extent of LN metastasis. The system to score the extent of metastasis in LNs was adapted from our previous study (20). As presented in **Figure 3A**, score 0 signifies undetectable macroscopic metastasis, scores 1 to 4 are the area of LNs covered by <5%, 5-15%, 15-25% and >25% melanoma cell infiltrate, respectively, and score 5 describes LNs that are full of melanoma cells. The extent of metastasis is presented in **Figure 3B-C** as scores per week, where week 1 is the week immediately after the first MRT session. The metastasis score in individual LNs and the average scores per day are shown in **Figure S2. Figure 3B** shows proportions of LNs with a given score. LNs with a higher score than in non-irradiated controls, were evident in the SF-MRT- and BB-irradiated cohorts at week 1 after irradiation. Metastatic progression was accelerated in the SF-MRT cohort over the BB cohort. At week 4, the majority of LNs in the SF-MRT cohort scored $\geq$3, and many LNs scored 5. Remarkably, the second MRT on D12 (week 2) delayed and even partially reversed metastasis progression. This is reflected in the similarity between the 2F-MRT diagram at week 4 and the SF-MRT diagram at week 2 (**Figure 3B**). The effect was long-lasting but not permanent. Metastasis continued to progress, such that the results for the 2F-MRT cohort at week 6 were similar to those of the SF-MRT diagram at week 4. These results were

confirmed by comparison of average scores of metastases presented in **Figure 3C**. The mean scores were not significantly different between the SF-MRT- and BB-irradiated cohorts, but the second MRT reduced the average score at weeks 2, 3 and 4 compared to the SF-MRT cohort (with statistical significance at weeks 3 and 4). At week 6, the average score in the 2F-MRT cohort increased.

Characteristics of LN metastasis in MRT-irradiated melanoma-bearing mice. Micro-tomography 3D-reconstructed images of metastatic LNs revealed a general accumulation of disseminated tumor cells on the superficial portions of the LNs (**Figure 4A**).

Biomarkers of viability and proliferation signify the ability of disseminated tumor cells to further metastasize. Epithelial-mesenchymal transition (EMT) is involved in the acquisition of aggressiveness and motility of cancer cells (22). Immunostaining of metastatic LNs for apoptosis and proliferation markers (cleaved caspase 3 and phospho-histone H3) revealed low incidence of apoptotic cells and presence of mitotic cells in the metastatic lesions (**Figure 4B** and **Figure S3A**) and the primary tumors (**Figure S3B**). Pan-cytokeratin (Pan-CK) was selected as an epithelial marker, and vimentin and fibronectin as mesenchymal markers. Metastatic lesions and primary tumors were pan-CK-positive, although the immunostaining intensity varied (**Figure 4B** and **Figure S3A-B**). The majority of metastases were vimentin-negative (LN1 in **Figure 4B**). In some LNs, the weak membrane-associated vimentin positivity was observed (LN2 in **Figure 4B** and **Figure S3A**). The weak fibronectin immunostaining was not typical and was associated with nuclei (**Figure 4B**), similar to the primary tumors (**Figure S3B**), as previously described in tumor cells (23). The weak positivity for mesenchymal markers could be the result of a long-term storage of paraffin blocks. Immunostaining intensity was much higher in freshly PFA-fixed

14

melanomas that were stored frozen prior to fixation (**Figure S3C-D**), with the same atypical nuclear positivity for fibronectin in non-irradiated tumors (**Figure S3C**), but with the cell membrane positivity in MRT-irradiated tumors (**Figure S3D**). Therefore, the expression of EMT markers in metastatic tumor cells indicates their potential to propagate further.

The second MRT modulates systemic and local immune responses

SF-MRT has been shown to induce a strong immune response in B16F10 melanomas (9). To understand whether the second MRT fraction can boost this response, and in search for candidate mediators of the observed metastasis regression, we compared plasma concentrations of cytokines involved in pro- and anti-inflammatory responses and tumor-infiltrating immune cell subpopulations in SF- and 2F-MRT cohorts.

2F-MRT-induced acute inflammatory response is mitigated by cytokines involved in chronic inflammation. Dynamic changes in the concentrations of 14 cytokines revealed statistical significance, as shown in **Figure 5.** Nineteen cytokines whose changes were not statistically significant, are shown in **Figure S4.** Two pro-inflammatory neutrophil-attracting cytokines, CXCL5 and CCL22, were significantly increased two days after the second MRT (D12), compared to levels in the SF-MRT cohort ($p<0.01$). Soon after, their concentrations declined. CXCL12 also increased compared to levels in the SF-MRT cohort ($p<0.05$ at D5). This increase relates to a recruitment of inflammatory cells, such as tumor-associated neutrophils (TANs), T-cells and CTLs. An increase in CCL11 after 2F-MRT was maintained at the later time-points ($p<0.01$ at D19 *vs.* D12 in the SF-MRT cohort), indicating an increased attraction of eosinophils.

15

Plasma concentrations of 5 cytokines statistically significantly decreased at one or more time-points in the 2F-MRT cohort, compared to the SF-MRT cohort. These included: CXCL10, which regulates cell growth, apoptosis and angiostatic effects; CCL19, which correlates with the tumor response; CCL20, which downregulates formation and function of lymphoid tissues and CCL24, which balances the recruitment of eosinophils to the tumor. There was a trend for a decrease in CCL25, which attracts tumor-associated macrophages (TAMs) and dendritic cells (DCs). The kinetics of these down-regulated cytokines was similar in both cohorts. There was a steady increase at the later time-points, indicating an attenuation of the acute inflammation, as CC-chemokine receptors are critical mediators of chronic inflammatory responses (24). IL-1β (which is produced by inflammatory macrophages and neutrophils) and IL-2 (which regulates proliferation of activated lymphocytes) exhibited a similar increase.

2F-MRT-induced recruitment of neutrophils and activation of local T-cells in the tumor microenvironment. To validate our findings related to the systemic cytokine modulation, ChipCytometry analysis, a high-plex, quantitative imaging platform with a single-cell resolution (25) was employed for a side-by-side comparison of the immune cell composition in SF- and 2F-MRT-irradiated tumors at the second day following the second fraction (D12). The detection strategy of immune cell subpopulations is illustrated in **Figure 6A-C**, and differences in immune cell lineages in the SF- and 2F-MRT cohorts compared to the parental populations are shown in **Figure 6D**.

TANs were significantly elevated ($p<0.05$) and total T-cells decreased ($p<0.05$) in the 2F-MRT-irradiated tumors. Importantly, a significantly higher frequency of activated T-cells was present in the survived T-cell population in the 2F-MRT group *vs.* the SF-

MRT group (p<0.05). A trend towards increased major histocompatibility complex class II (MHCII) and recruitment of monocytes was observed in the 2F-MRT group, as well as a trend towards decreased recruitment of DCs and TAMs.

Overlays of gated populations for T-cell subsets are displayed in the T-distributed stochastic neighbor embedding (tSNE) space for one randomly selected sample of the SF-MRT and 2F-MRT groups (**Figure 6E**, images on the right). t-SNE density plots in **Figure 6E** (images on the left) shows an overview of the distribution of the whole cells detected on the tissue slice. The overlays (images on the right) were manually gated, and each single cell was color-coded. The tSNE technique allows for visualization of complex multi-dimensional data in fewer dimensions while still maintaining the structure of the data. In both samples, distinct separation of T-cell subpopulations is evident in different regions of the map, as well as their overlay of the region covered by T-cells. The larger distribution of activated T-cells (dark blue overlay) over the total T-cells in the 2F-group *vs*. the SF-MRT group confirms the quantitative data.

Discussion

Synchrotron-generated X-ray MRT provides better tumor control in animal models than BB irradiation (8), with a major benefit being the significantly reduced damage to normal tissues within the field (3,26). We explored the ability of fractionated MRT to attenuate growth and progression of radioresistant B16F10 murine melanoma and evaluated the metastatic spread in cervical sentinel LNs after SF- and 2F-MRT treatment. For the first time we present a comprehensive analysis of locoregional metastases after the use of synchrotron radiation. We measured plasma concentrations of 34 pro- and anti-inflammatory cytokines in blood samples collected on different days after SF- and 2F-MRT irradiations, to understand which immune factors support regression of both primary tumor and metastasis after the second MRT treatment. We validated the data by comparing the immune cell composition in SF- and 2F-MRT-treated tumors by ChipCytometry. This report is the largest study of MRT-induced immune responses to date.

Characteristics of synchrotron MRT. MRT features an array of microscopic (μm-range) parallel planar beams of synchrotron generated X-rays delivered at exceptionally high dose rates up to 16 kGy/s (27). Supraclinical hecto-Gy doses can, therefore, be delivered in milliseconds, i.e. in FLASH mode (>100 Gys^{-1}) (28). Both spatial fractionation and FLASH RT reduce normal tissue toxicity and increase the therapeutic index of the treatment by sparing normal tissue surrounding the tumor, however, the underlying mechanisms likely differ. For MRT, the dose gradient generated by the alternating peak and valley areas, evokes bystander effects and vascular disruption specific to the areas of the high doses in tumors. The same dose gradient has been recently proposed as a possible cause of a strong local and

18

systemic anti-tumor immune responses (reviewed in (29) and (9)). In MRT, the contribution of the FLASH delivery component is not yet clear, nor is the status of tumor oxygenation, as many studies indicate that the mechanism of action of FLASH RT is oxygen dependent. The influence of oxygen on downstream biological effects however, still requires further investigation in order to reach a consensus (30).

2F-MRT improves local control of B16F10 melanoma. A previous study demonstrated that normally radioresistant B16F10 melanomas showed an excellent response to a single MRT treatment and more efficient compared to a single 6.2 Gy BB irradiation (8). At 9-10 days after irradiation, the volume of responsive tumors reached a nadir, prompting us to deliver at this specific time the second MRT fraction, to boost the tumor control. The 2F regimen significantly delayed tumor progression. The tumors of the 2F-MRT cohort did not reach the size of the SF-MRT cohort at the endpoint of the experiment. Considering that the average size of the tumors at the time of receiving the second MRT was greater than at D0, when the first MRT was administered, the tumor growth delay obtained with the 2F regimen exceeded our expectations. The outstanding treatment success of 2F-MRT can be attributed to not only the direct killing of melanoma cells, but also to the additive biological effects reported in earlier publications, e.g. disruptive effect on the immature tumor vasculature (3,8,31) and the anti-tumor immune response (8,9). A limitation of this study is that in addition to temporal fractionation, there are two other factors that may have contributed to the excellent tumor control achieved. First, the total radiation dose administered differs between cohorts: the 2F-MRT cohort received twice the dose of the SF-MRT group. Second, the radiation dose was spatially distributed differently at the target site: the 2F-MRT overlapped the SF-MRT

at a 90° angle, creating a cross-hatched pattern. Further studies are needed to determine the impact of each of these variables on the final treatment efficacy.

Association between RT and metastasis. Tumor recurrence and distant metastases are common even after successful RT with curative-intent for various cancers (12). Animal studies have shown that conventional RT can increase the risk of metastasis (13,32). This could be related to the release of viable tumor cells into the bloodstream, possibly through radiation-induced disruption of tumor architecture and vasculature which could facilitate the escape of cells with metastatic potential from the primary tumor (14). In fact, tumor cells have been found in the bloodstream of some cancer patients after commencement of RT (33). An association between the RT fractionation schedule and the subsequent risk of distant metastasis has been reported in a randomized clinical trial that compared Continuous Hyperfractionated Accelerated RT (CHART) to conventional RT in locally-advanced lung cancer (34). In addition to improving survival and local control, CHART resulted in a reduction in distant metastasis (34). It is hypothesized that because CHART was delivered in 3 fractions per day, tumor cells would have acquired more damage thus be less capable to survive and metastasize.

Depending on the irradiation schedule, MRT can contribute to, or reduce locoregional metastasis. We have previously shown that MRT effects are mediated by vascular toxicity (3,31). In combination with sublethal cellular damage in the valley areas between the microbeams (e.g., 6.5 Gy in this study), an opportunity exists for tumor cells or cell clusters to escape by extravasation into the circulation and to disseminate. Alternatively, or in parallel, they can enter the lymphatic system. Potentially, these disseminated tumor cells can be more aggressive, motile and metastatic than non-irradiated cells (14).

20

Dissection of B16F10 melanoma-bearing mice with advanced primary tumors that were either non-irradiated or irradiated with MRT and BB, revealed LN-positivity in nearly all animals. However, it is noteworthy that in our recent study (10), delivery of MRT in three daily fractions of 133.41 Gy peak-dose, resulted in complete ablation of 50% melanomas, with no locoregional or distant metastasis in these animals at 18 months after treatment. We are conscious of the fact, however, that MRT efficacy cannot be attributed to temporal fractionation alone, and that the crossing of the MRT arrays can be another contributing factor (this issue has been discussed in (10)). Nevertheless, this outstanding result prompted us to examine the comprehensive LN collection with the B16F10 melanoma model.

Here we report that both SF-MRT and BB accelerated formation of locoregional macro-metastases (60% of positive nodes after MRT and 22.2% after BB *vs.* 7.1% in control mice at D2) to a comparable extent at later times. Intra-nodal metastasis affected LNs of various sizes, confirming clinical data (35). However, only in the SF-MRT-irradiated cohort, we observed unusually enlarged metastatic LNs in some animals. The metastatic tumor cells were alive, dividing, and expressed EMT markers, suggesting their potential to propagate further (22). Remarkably, the second MRT produced a very pronounced reduction in metastasis that lasted 5 weeks. The low-dose scatter radiation alone in each LN is estimated to be in the range of 34-50 mGy, that would not generate any lethal effect on the tumor cells. The immune system-mediated abscopal effect, where local irradiation causes changes in tissues and organs outside the field of irradiation, including out-of-field, non-irradiated tumor, is another conceivable explanation.

Anti-metastatic abscopal effect. In the clinic, reports of spontaneous abscopal effects are rare. According to Ko et al (36), abscopal responses for conventional RT are

21

more prominent following larger doses, supporting the use of hypofractionation. The hypofractionated regimen has been optimized in the pre-clinical setting, with three daily doses of 8 Gy proving most effective in inducing regression of a second non-irradiated tumor (37). Hypofractionated SFRT delivered with a conventional radiation source to one primary mouse lung carcinoma effectively reduced another non-irradiated tumor (38). The robust generation of the abscopal effect by hypofractionation and SFRT with high doses aligns with our finding that the second MRT fraction successfully reduced locoregional metastasis, and with the observed lack of metastasis when three daily MRT fractions were applied (10).

Studies have reported that the immune system is an integral component of the anti-tumor abscopal response and that activation of the immune system, commonly using checkpoint inhibitors against CTLA-4, PD-1 and OX40 in combination with local RT, was able to induce growth suppression in a second non-irradiated primary tumor (37,39). It is therefore proposed that local RT can incite systemic disease control, i.e. 'in-situ vaccination' that is especially relevant to stereotactic radiosurgery and SFRT, such as MRT. Immune responses following irradiation of B16F10 melanoma with a single MRT dose have been documented. Specifically, increases in the plasma concentrations of MCP1, MIP1α and MIP1β, which are associated with recruitment of monocytes/macrophages were observed. This was corroborated by infiltration of the tumor microenvironment with macrophages, NK cells, CD4+ T-helpers and CD8+ CTLs (8). A unique gene signature for an 'MRT-induced immune effect' has been underlined, i.e., *Ccl9* and *Rsad2* overexpression in MRT-irradiated tumors compared to BB-irradiated tumors (9). Ccl9 is a chemokine that recruits myeloid progenitor cells to the tumor microenvironment, and Rsad2 is triggered by the type-I INF pathway that has been shown to activate abscopal effects (9).

2F-MRT triggers an anti-tumor immune response. In search for factors that generated the anti-tumor/anti-metastatic response after the second MRT, we measured plasma concentrations of 34 pro- and anti-inflammatory cytokines in cohorts of mice that received one or two MRT fractions. The second MRT treatment significantly increased plasma levels of neutrophil-attracting chemokines CXCL5 and CXCL12 (40,41), contributing to their long-term immunomodulatory effects. TANs may, under the influence of the local tumor microenvironment and irradiation, obtain an anti-tumor (N1) or pro-tumor (N2) phenotype, and can either suppress or support tumor growth, and metastasis progression (42). In TANs, CXCL5 induces increased production of cytotoxic reactive oxygen species (ROS), promoting their anti-tumor properties (43). Similarly, CXCL12 induces increased ROS production and enhances respiratory burst activity of N1 neutrophils in inflamed tissues (44). Accordingly, elevated plasma levels of CXCL5 and CXCL12 could result in the higher presence of N1 neutrophils within the tumor microenvironment at early stages of tumor progression and, therefore, contribute to the alleviation of melanoma growth and progression in 2F-MRT-treated animals. Indeed, elevated *in-situ* TAN frequencies in 2F-MRT-irradiated tumors were confirmed by ChipCytometry at two days post-exposure, compared to the SF-MRT-irradiated tumors.

Activity of adaptive immune cells, including T-helpers and CTLs, also promotes anti-tumor immunity (45). As recently demonstrated by several groups, single MRT treatment significantly increased the total number of tumor-infiltrating T-cells, resulting in attenuated growth of murine melanoma and breast cancer (8,46). Here, we demonstrated that 2F-MRT significantly increased plasma levels of CCL22 that recruits CCR4-expressing CD8+ CTLs and CD4+ T-helpers to the tumor (47). While an overall population of tumor-infiltrating T-cells was quickly destroyed by ablative

peak doses of the second MRT, there were significantly more activated T-cells in 2F-MRT-exposed tumors, compared to their SF-MRT-exposed counterparts. These survivors are likely to be located in the valley regions, where the dose was not high enough to kill all T-cells; a unique characteristic of a SFRT (2,27). Additionally, MRT can spare some T-cells due to the FLASH-effect which reduces ROS-mediated cellular damage by rapidly consuming local oxygen (28,48). Based on the observed trend of increasing MHCII+ cells, these activated T-cells are likely to exhibit increased response to antigen presentation and amplification of T-cell immunity at sites of radiation-induced inflammation. Antigen-presenting cells could travel to regional LNs and other organs and prime T-cells, which would attack metastatic tumors; a proposed mechanism underlying abscopal effects (49). The proposed mechanisms behind the efficacy of the second MRT fraction are summarized in **Figure 7**. The fundamental radiobiological question of the mechanisms of cell death that trigger a spectrum of immune responses after extremely heterogeneous doses delivered by MRT is yet to be addressed. It is likely that MRT may result in different types of cell death in the same irradiation field supported by multiple signal transduction cascades with underlying dysregulation of redox homeostasis and bioenergetic metabolism and a loss of Ca^{2+} homeostatic control (50,51).

To confirm the importance of immune cell subpopulations for modulation of anti-tumor immunity, future studies should determine their exact phenotype and function in individual MRT-treated tumors in correlation with local tumor control and the systemic response to radiation.

Conclusions. The importance of our study resides in the fact that radioresistant B16F10 melanoma is susceptible to MRT treatment, while conventional RT is not effective due to inherent radioresistance of the tumor. Moreover, spatially fractionated

microbeams delivering ultra-high doses of radiation efficiently modulate systemic and local immune responses over a wide range of doses. Thus, MRT offers a new treatment formula with the potential to systematically cure metastases. This would be a turning point in the treatment options for patients with metastatic disease as their prognosis still remains poor at the moment of first diagnosis. The robust endpoints exploited in this study will be utilized in future MRT experimentation aiming to define the fractionation schedule for the best local and locoregional control, as well as for management of distant metastasis.

We are confident that in the next few years we will witness the first MRT clinical trials, especially with the first veterinary dog trials underway at the European Synchrotron (52). Furthermore, with the awareness that compact sources for MRT delivery are essential for more widespread use, we are planning to investigate and compare the effects of synchrotron-generated MRT *vs.* MRT generated by non-synchrotron sources. It is essential to understand how dependent MRT efficacy is on synchrotron delivery and to find alternative X-rays sources that would make MRT more available to cancer patients worldwide.

References

1. Griffin RJ, Ahmed MM, Amendola B, et al. Understanding high-dose, ultra-high dose-rate and , spatially fractionated radiotherapy. *Int J Radiat Oncol Biol Phys* 2020.

2. Schultke E, Balosso J, Breslin T, et al. Microbeam radiation therapy - grid therapy and beyond: A clinical perspective. *Br J Radiol* 2017;90:20170073.

3. XXX

4. Trappetti V, Fernandez-Palomo C, Smyth L, et al. Synchrotron microbeam radiotherapy for the treatment of lung carcinoma: A pre-clinical study. *Int J Radiat Oncol Biol Phys* 2021.

5. Kauffmann A, Rosselli F, Lazar V, et al. High expression of DNA repair pathways is associated with metastasis in melanoma patients. *Oncogene* 2008;27:565-73.

6. Wu L, Hu Z, Huang Y, et al. Radiation changes the metabolic profiling of melanoma cell line b16. *PLoS One* 2016;11:e0162917.

7. Lugade AA, Moran JP, Gerber SA, et al. Local radiation therapy of b16 melanoma tumors increases the generation of tumor antigen-specific effector cells that traffic to the tumor. *J Immunol* 2005;174:7516-23.

8. XXX

9. XXX

10. XXX

11. Keung EZ, Gershenwald JE. The eighth edition american joint committee on cancer (ajcc) melanoma staging system: Implications for melanoma treatment and care. *Expert Rev Anticancer Ther* 2018;18:775-784.

12. Mac Manus MP, Hicks RJ, Matthews JP, et al. Metabolic (fdg-pet) response after radical radiotherapy/chemoradiotherapy for non-small cell lung cancer correlates with patterns of failure. *Lung Cancer* 2005;49:95-108.

13. Camphausen K, Moses MA, Beecken WD, et al. Radiation therapy to a primary tumor accelerates metastatic growth in mice. *Cancer Res* 2001;61:2207-11.

14. Martin OA, Anderson RL, Narayan K, et al. Does the mobilization of circulating tumour cells during cancer therapy cause metastasis? *Nat Rev Clin Oncol* 2017;14:32-44.

15. Mathias TJ, Chang KT, Martin SS, et al. Gauging the impact of cancer treatment modalities on circulating tumor cells (ctcs). *Cancers (Basel)* 2020;12.

16. Strom T, Torres-Roca JF, Parekh A, et al. Regional radiation therapy impacts outcome for node-positive cutaneous melanoma. *J Natl Compr Canc Netw* 2017;15:473-482.

17. Danish HH, Patel KR, Switchenko JM, et al. The influence of postoperative lymph node radiation therapy on overall survival of patients with stage iii melanoma, a national cancer database analysis. *Melanoma Res* 2016;26:595-603.

18. Budach W, Kammers K, Boelke E, et al. Adjuvant radiotherapy of regional lymph nodes in breast cancer - a meta-analysis of randomized trials. *Radiat Oncol* 2013;8:267.

19. Engel J, Emeny RT, Holzel D. Positive lymph nodes do not metastasize. *Cancer Metastasis Rev* 2012;31:235-46.

20. XXX

21. XXX

22. Burr R, Gilles C, Thompson EW, et al. Epithelial-mesenchymal plasticity in circulating tumor cells, the precursors of metastasis. *Adv Exp Med Biol* 2020;1220:11-34.

23. Zerlauth G, Wesierska-Gadek J, Sauermann G. Fibronectin observed in the nuclear matrix of hela tumour cells. *J Cell Sci* 1988;89 (Pt 3):415-21.

24. White GE, Iqbal AJ, Greaves DR. Cc chemokine receptors and chronic inflammation--therapeutic opportunities and pharmacological challenges. *Pharmacol Rev* 2013;65:47-89.

25. Hennig C, Adams N, Hansen G. A versatile platform for comprehensive chip-based explorative cytometry. *Cytometry A* 2009;75:362-70.

26. van der Sanden B, Brauer-Krisch E, Siegbahn EA, et al. Tolerance of arteries to microplanar x-ray beams. *Int J Radiat Oncol Biol Phys* 2010;77:1545-52.
27. Brauer-Krisch E, Serduc R, Siegbahn EA, et al. Effects of pulsed, spatially fractionated, microscopic synchrotron x-ray beams on normal and tumoral brain tissue. *Mutation research* 2010;704:160-6.
28. Bourhis J, Montay-Gruel P, Goncalves Jorge P, et al. Clinical translation of flash radiotherapy: Why and how? *Radiotherapy and oncology : journal of the European Society for Therapeutic Radiology and Oncology* 2019;139:11-17.
29. XXX
30. Wilson JD, Hammond EM, Higgins GS, et al. Ultra-high dose rate (flash) radiotherapy: Silver bullet or fool's gold? *Front Oncol* 2019;9:1563.
31. XXX
32. Park JK, Jang SJ, Kang SW, et al. Establishment of animal model for the analysis of cancer cell metastasis during radiotherapy. *Radiat Oncol* 2012;7:153.
33. Martin OA, Anderson RL, Russell PA, et al. Mobilization of viable tumor cells into the circulation during radiation therapy. *Int J Radiat Oncol Biol Phys* 2014;88:395-403.
34. Saunders M, Dische S, Barrett A, et al. Continuous hyperfractionated accelerated radiotherapy (chart) versus conventional radiotherapy in non-small-cell lung cancer: A randomised multicentre trial. Chart steering committee. *Lancet* 1997;350:161-5.
35. Schrembs P, Martin B, Anthuber M, et al. The prognostic significance of lymph node size in node-positive colon cancer. *PLoS One* 2018;13:e0201072.
36. Ko EC, Benjamin KT, Formenti SC. Generating antitumor immunity by targeted radiation therapy: Role of dose and fractionation. *Adv Radiat Oncol* 2018;3:486-493.
37. Vanpouille-Box C, Alard A, Aryankalayil MJ, et al. DNA exonuclease trex1 regulates radiotherapy-induced tumour immunogenicity. *Nat Commun* 2017;8:15618.
38. Kanagavelu S, Gupta S, Wu X, et al. In vivo effects of lattice radiation therapy on local and distant lung cancer: Potential role of immunomodulation. *Radiation research* 2014;182:149-62.
39. Esposito A, Criscitiello C, Curigliano G. Immune checkpoint inhibitors with radiotherapy and locoregional treatment: Synergism and potential clinical implications. *Curr Opin Oncol* 2015;27:445-51.
40. Soler-Cardona A, Forsthuber A, Lipp K, et al. Cxcl5 facilitates melanoma cell-neutrophil interaction and lymph node metastasis. *J Invest Dermatol* 2018;138:1627-1635.
41. Isles HM, Herman KD, Robertson AL, et al. The cxcl12/cxcr4 signaling axis retains neutrophils at inflammatory sites in zebrafish. *Front Immunol* 2019;10:1784.
42. Takeshima T, Pop LM, Laine A, et al. Key role for neutrophils in radiation-induced antitumor immune responses: Potentiation with g-csf. *Proc Natl Acad Sci U S A* 2016;113:11300-11305.
43. Forsthuber A, Lipp K, Andersen L, et al. Cxcl5 as regulator of neutrophil function in cutaneous melanoma. *J Invest Dermatol* 2019;139:186-194.
44. Hartl D, Krauss-Etschmann S, Koller B, et al. Infiltrated neutrophils acquire novel chemokine receptor expression and chemokine responsiveness in chronic inflammatory lung diseases. *J Immunol* 2008;181:8053-67.
45. Mantovani A, Cassatella MA, Costantini C, et al. Neutrophils in the activation and regulation of innate and adaptive immunity. *Nat Rev Immunol* 2011;11:519-31.
46. Yang Y, Swierczak A, Ibahim M, et al. Synchrotron microbeam radiotherapy evokes a different early tumor immunomodulatory response to conventional radiotherapy in emt6.5 mammary tumors. *Radiotherapy and oncology : journal of the European Society for Therapeutic Radiology and Oncology* 2019;133:93-99.
47. Cho S, Koizumi K, Takeno N, et al. Anti-tumor effect of combining cc chemokine 22 and an anti-cd25 antibody on myeloma cells implanted subcutaneously into mice. *Mol Med Rep* 2009;2:773-7.

48. Montay-Gruel P, Acharya MM, Petersson K, et al. Long-term neurocognitive benefits of flash radiotherapy driven by reduced reactive oxygen species. *Proc Natl Acad Sci U S A* 2019;116:10943-10951.

49. Xing D, Siva S, Hanna GG. The abscopal effect of stereotactic radiotherapy and immunotherapy: Fool's gold or el dorado? *Clin Oncol (R Coll Radiol)* 2019;31:432-443.

50. Orrenius S, Zhivotovsky B, Nicotera P. Regulation of cell death: The calcium-apoptosis link. *Nat Rev Mol Cell Bio* 2003;4:552-565.

51. Galluzzi L, Vitale I, Aaronson SA, et al. Molecular mechanisms of cell death: Recommendations of the nomenclature committee on cell death 2018. *Cell Death Differ* 2018;25:486-541.

52. Adam JF, Balosso J, Bayat S, et al. Towards neuro-oncologic clinical trials of high dose rate synchrotron microbeam radiation therapy: First treatment of a spontaneous canine brain tumor.: First microbeam treatment of canine brain tumor. *Int J Radiat Oncol Biol Phys* 2022.

Figure captions

Figure 1. MRT double-treatment significantly enhances melanoma regression.
(A) Experimental scheme. Mice from the 'SF-MRT' group (N=14) were irradiated once (at 11th day after tumor implantation, D0), with 396-Gy peak dose while mice from the '2F-MRT' group (N=20) received two irradiations with 396-Gy peak dose (at 11th and 21st day after tumor implantation, respectively, D0 and D10 post-first MRT session). **(B)** Tumor volume curves of MRT single (pink, 28 tumors) and MRT double (blue, 40 tumors)-irradiated melanoma-bearing mice showing significantly enhanced melanoma regression after the second MRT irradiation. The already published tumor control data for BB irradiations and non-irradiated controls (8) are also included as dotted lines for comparison. Data presented as mean tumor volume ± SEM; *p=0.0081; ****p<0.0001 (two-way ANOVA multiple comparison test). **(C)** Categorization of melanomas according to their response to SF-MRT; non-shrunken tumors (partial response) and tumors exhibiting shrinkage and growth delay (response). **(D)** Categorization of melanomas according to their response to 2F-MRT; non-shrunken tumors (partial response), tumors exhibiting shrinkage and growth delay (response) and tumors exhibiting complete remission (complete response).
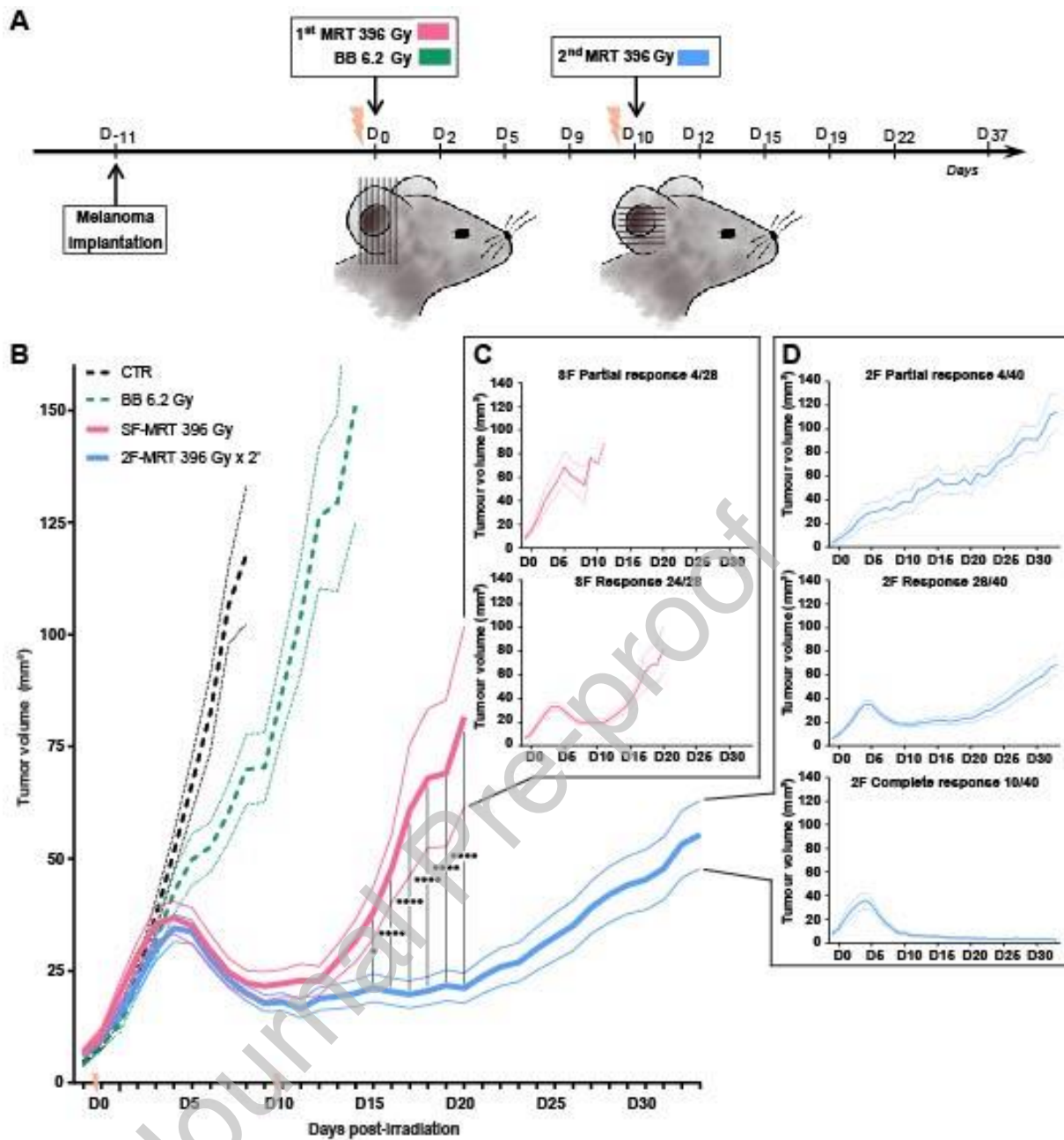
Figure 2. Size of sentinel LNs prior to and post-irradiations. Each dot represents a single LN (length, mm). They are grouped by cohort: non-irradiated control (CTR), BB, SF-MRT and 2F-MRT, and by week: week 1, 1-7 days post post-first MRT session; week 2, 8-14 days; week 3, 15-21 days; week 4, 22-28 days; week 6 is presented by D37, where the experiment was stopped, and all surviving mice were culled. LNs in the control group were also measured one day prior to irradiation (D-1).

Black horizontal bars show the median size of the experimental group. *p=0.0142 (Kruskal-Wallis multiple comparison test within each group).
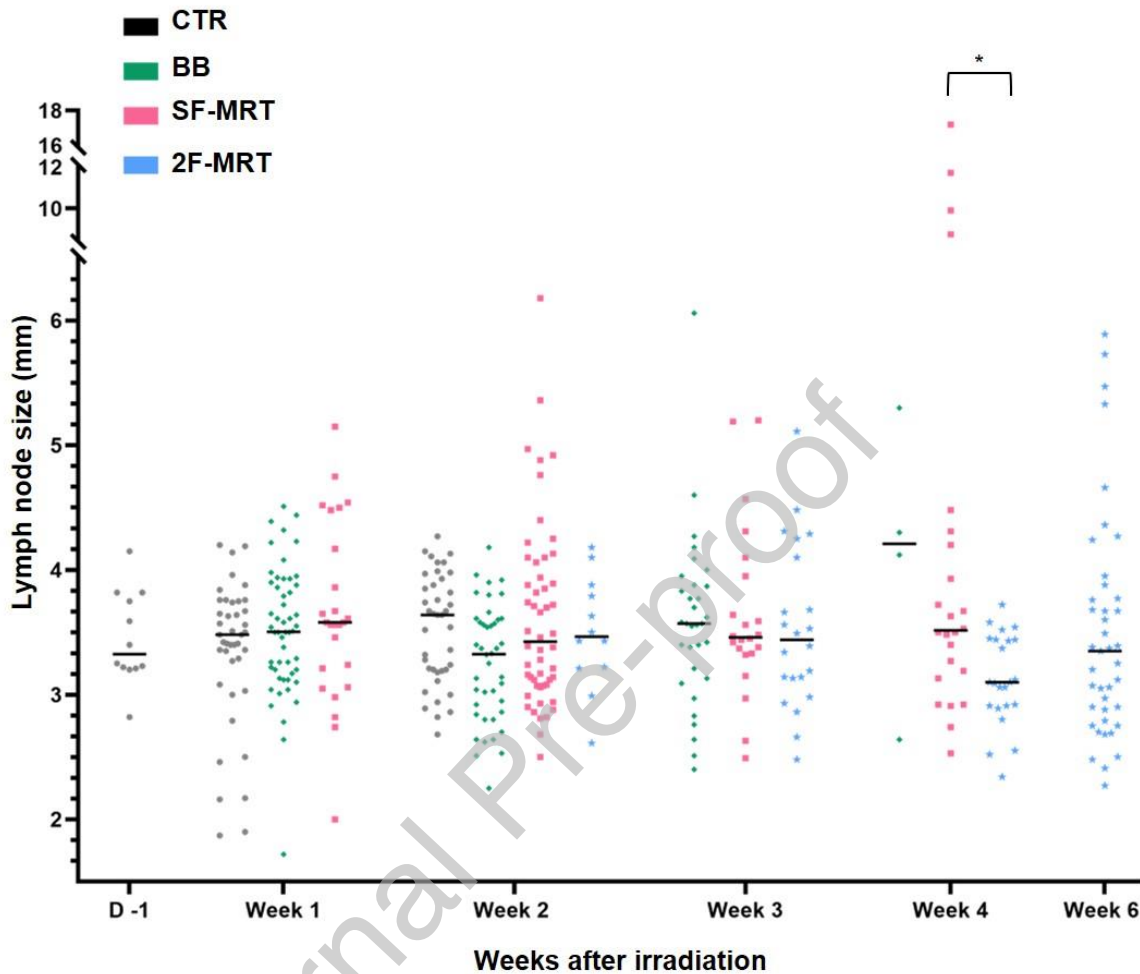
Figure 3. Extent of melanoma cells occupying the dissected cervical sentinel LNs. (A) Representative images of LNs to illustrate the scoring system according the burden of metastatic black melanoma tissue in each LN. The scoring has been described previously (20), where score 0 signifies no metastasis, scores 1 to 4 are the area of LNs covered by < 5%, 5-15%, 15-25% and >25% melanoma cell infiltrate, respectively, and score 5 defines large LNs (4-9 mm, in one case 17.2 mm) that are filled with melanoma cells. **(B)** Fractions of LNs with a given score. LNs are grouped by cohort (non-irradiated control (CTR), BB, SF-MRT and 2F-MRT), and by time post-first MRT session. LNs in the control group were also measured one day prior

31

to irradiation. **(C)** Average metastatic scores grouped by experimental cohort and by time post-first MRT session. LNs in the control group were also measured one day prior to irradiation (D-1). Data shown as mean score $\pm$ SD. *p=0.0186; ****p<0.0001 (one-way ANOVA multiple comparison test).
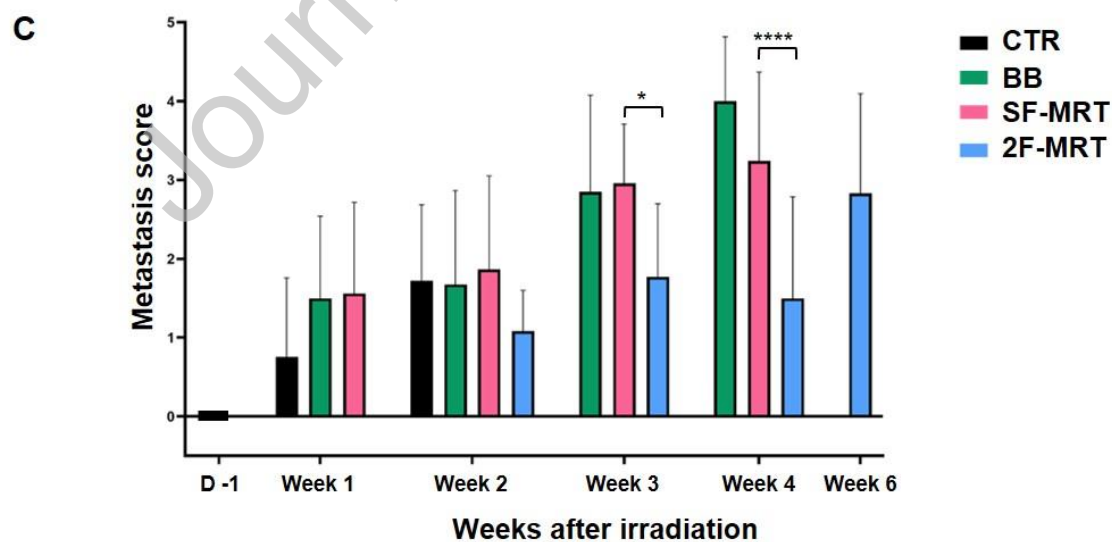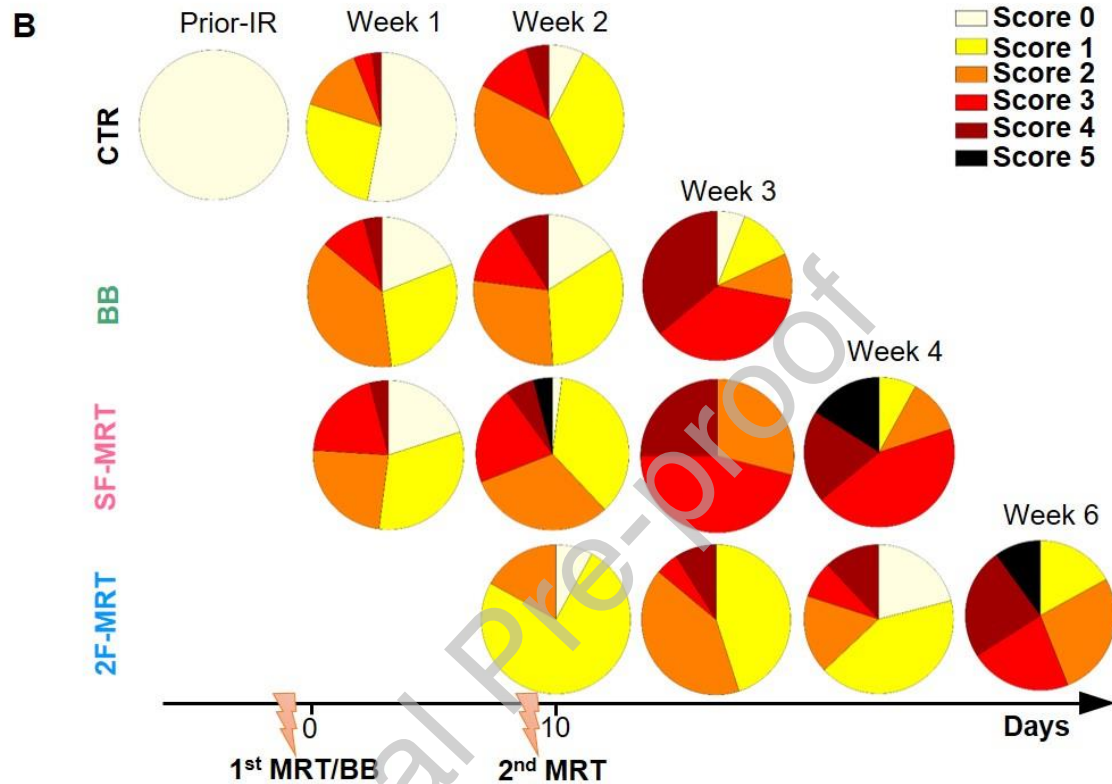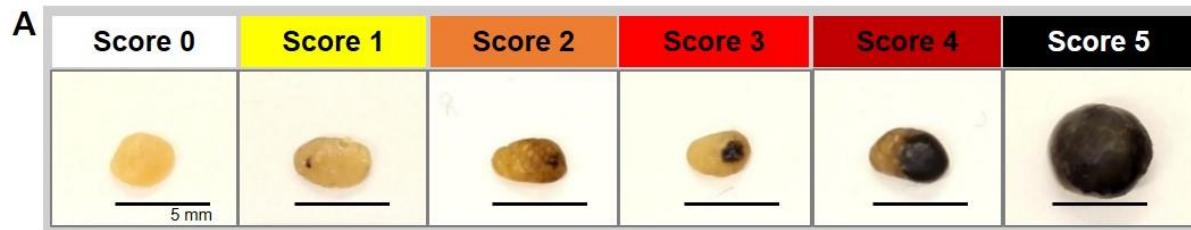
Figure 4. Characteristics of LN metastasis. (A) A representative low score LN (top panel) and a high score LN (low panel) harvested from mice with irradiated primary tumors. From left to right: images of segmented metastasis in micro-tomography 3D-reconstructed images (frontal view and two different lateral views); macroscopic photographs of the same LNs; and microscopic images of histological sections from the same LNs immunostained for anti-melan A, at two different magnifications. **(B)** Viability and motility markers of tumor cells in LN metastasis. Microscopic images of histological sections of two LNs harvested from mice with MRT-irradiated primary tumors are shown at two different magnifications. Sections were immunostained for cleaved caspase-3 (CC3), phospho-histone H3 (PH3), pan-cytokeratin (pan-CK), vimentin and fibronectin. Melan A was used to identify the location of melanoma cells. Brown, peroxidase immunostaining; blue, nuclei counterstained with hematoxylin; black dots, melanin.
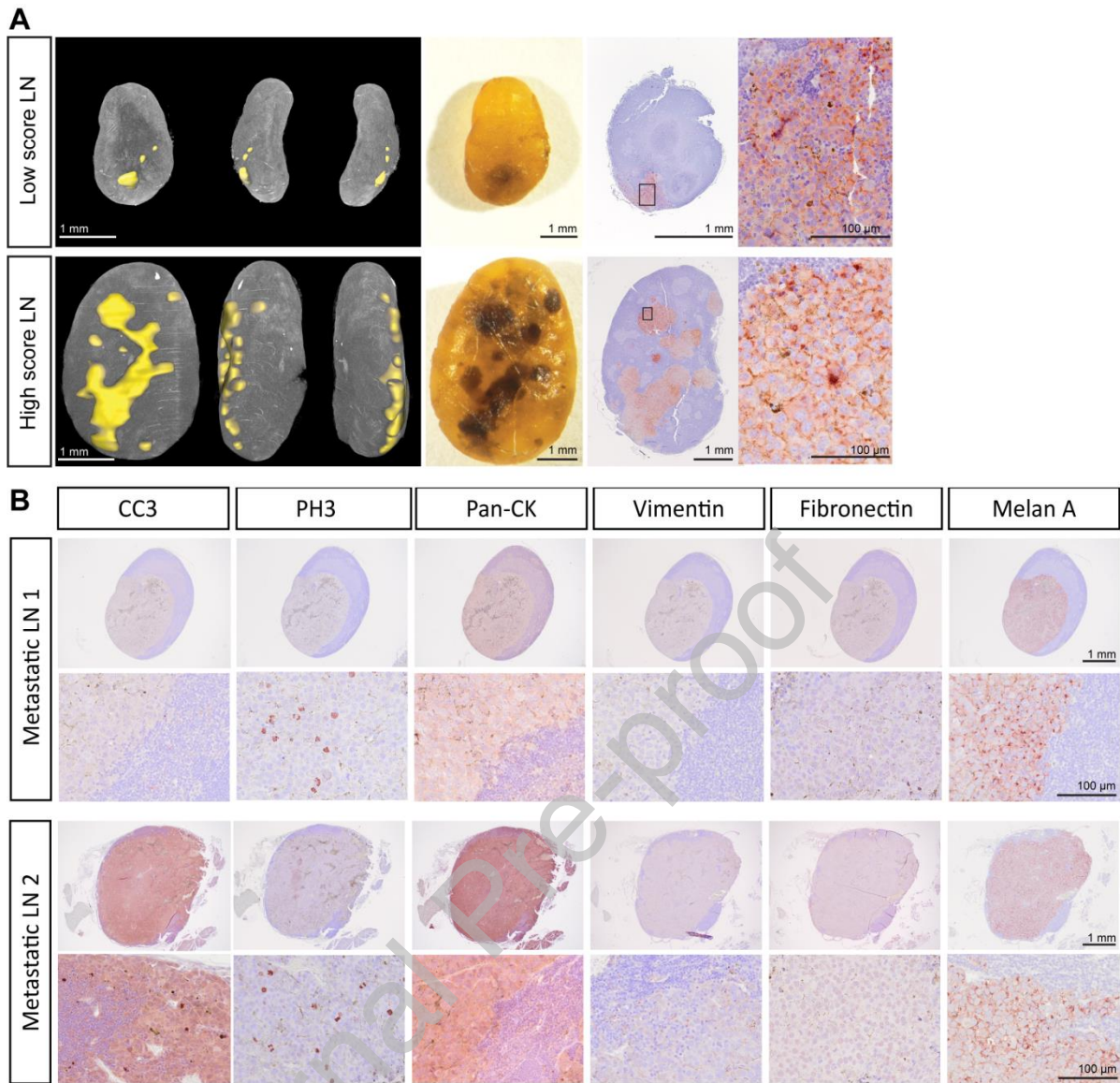
Figure 5. Modulations of 14 cytokines in melanoma-bearing mice irradiated with a single MRT fraction (SF) or double MRT fractions (2F). Plasma concentrations were measured by Bio-Plex immunoassay in samples of melanoma-bearing animals collected after SF-MRT (pink bars, D2-12) and 2F-MRT (blue bars, D12-22). N=5 mice per group per time point (D12 has N=4). Data shown as a mean concentration ± SD; *p < 0.05; **p < 0.01 (Kruskal–Wallis non-parametric multiple comparison test).
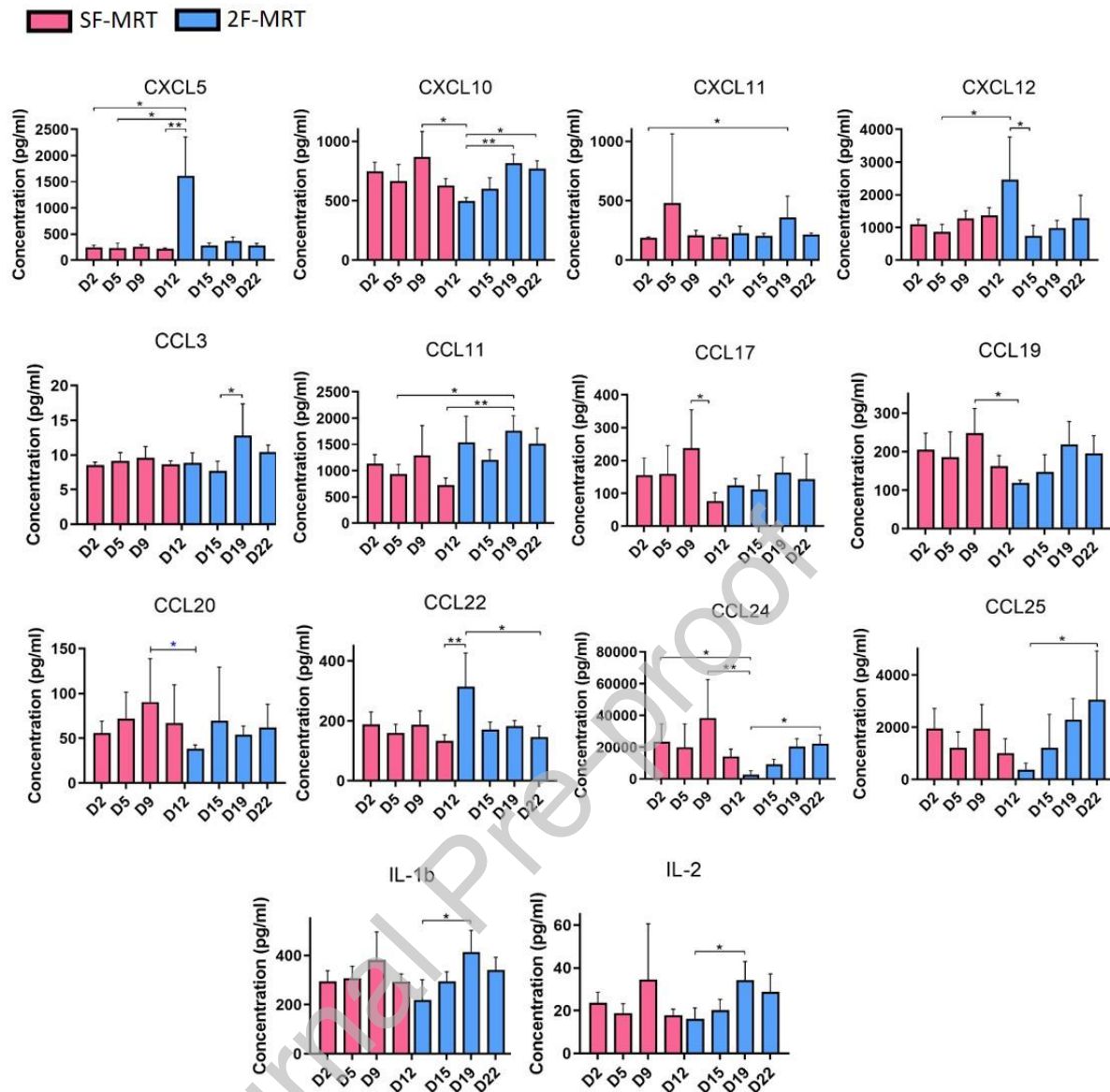
Figure 6. Analysis of the primary tumor immune cell lineages by ChipCytometry. **(A)** Schematic representation of the ChipCytometry workflow. OCT-frozen samples of SF-MRT- and 2F-MRT-irradiated tumors were subject to a comparative analysis. Six µm-thick tissue sections were loaded onto microfluidic chips and preserved by fixation. The samples were immunostained directly on the chips using fluorescently labelled antibodies via microfluidics, at 3-4-plex. The chips were imaged and then photobleached to remove a fluorescent signal for the next cycle of immunostaining. **(B)** Example of one melanoma section employed for the

36

multiplex analysis stained with DNA stain Hoechst 33342. **(C)** Phenotyping strategy for detection of the major tumor immune cell populations in high-resolution images acquired in four different fields of sections of MRT-irradiated tumors. Fields 1, 2, 3 and 4 correspond to the areas selected in panel **(C)**. **(D)** Quantification of the immune cell populations and relative sub-populations in two groups of tumors, exposed to SF-MRT, on D12 (pink bars), and exposed to 2F-MRT, on D12, i.e., at the second day post-second MRT irradiation (blue bars). The percentage of a given subpopulation is calculated over the parental population. From left to right and from the top to the bottom of the panel, fractions for the following cells are presented: leucocytes and MHCII + cells calculated over total immune cells; TANs, DCs, B-cells and T-cells calculated over leucocytes; T-helpers, CTLs, T-regs and activated T-cells calculated over total T-cells; myeloid cells calculated over leucocytes; monocytes and TAMs gated over myeloid cells and M2-like TAMs calculated over total TAMs. M1-like TAMs were not detected. The definition of each lineage in presented in Supplementary Materials and Methods. N=5 tumors per group per time point. Data shown as a mean % ± SD; *$p < 0.05$; **$p < 0.01$ (nonparametric Mann–Whitney test). **(E)** t-SNE density plots on the left and representation of overlaid gated T-cell subsets over total T-cells and leucocytes on the right. Top row, a randomly selected sample form the SF-MRT group; bottom row, a randomly selected sample from the 2F-MRT group.
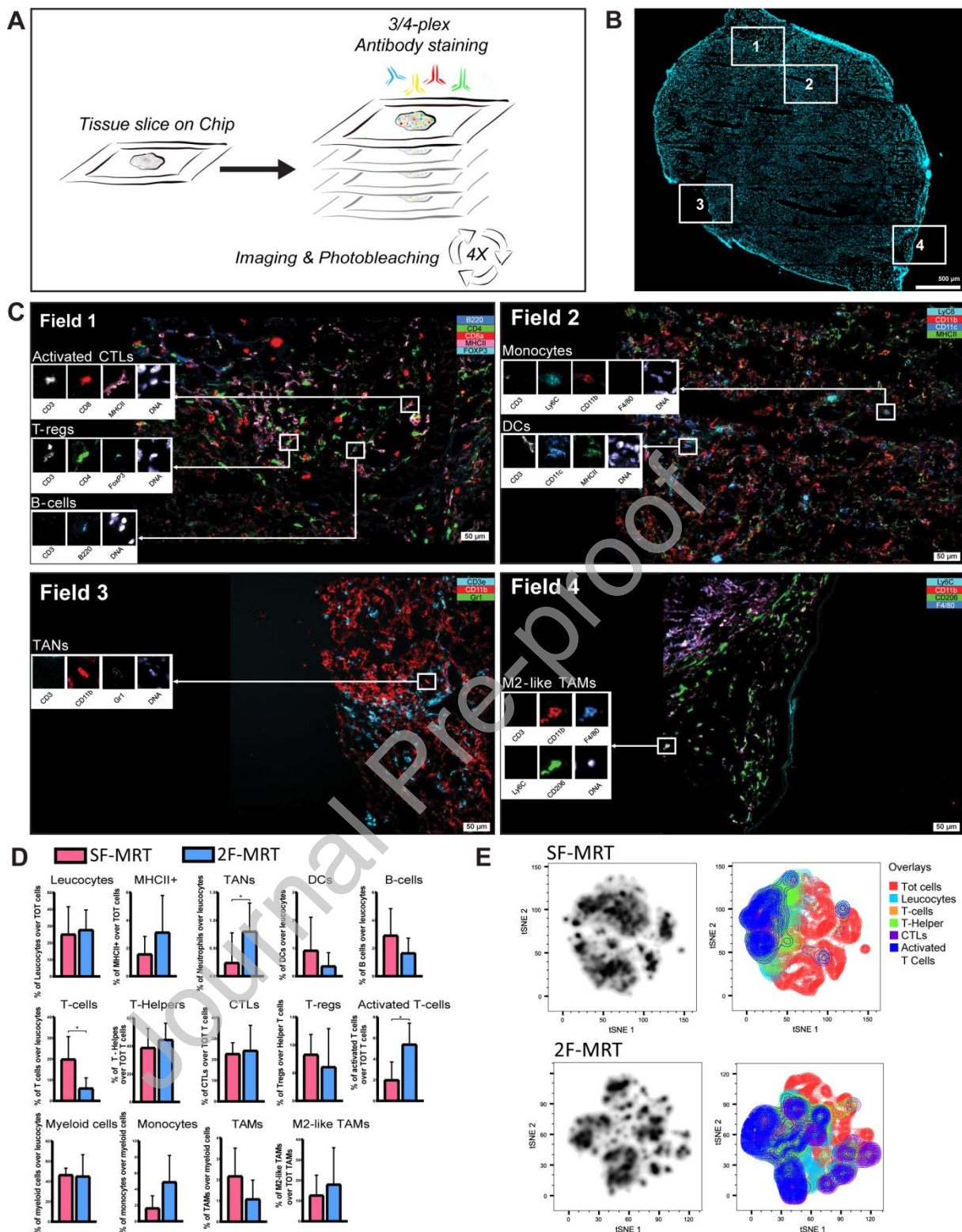
Figure 7. Comparison of biological events following single *vs.* double exposure of B16F10 melanoma to MRT. Single exposure to MRT (left panel) significantly delays primary tumor growth compared to BB irradiation or unirradiated controls. It also sensitizes radioresistant melanoma to radiation treatment and triggers

38

intratumoral infiltration of immune cells, such as monocytes and T cells (8). However, SF-MRT, as well as BB irradiation, accelerates the formation of locoregional metastases in superficial cervical lymph nodes. A double fraction of MRT (right panel) elicits a significant delay in primary melanoma growth with respect to a single-fraction and reduces out-of-field, locoregional progression of metastases. The unique geometry of MRT results in a dose gradient that, in addition to its delivery in FLASH mode, increases immune cell sparing in the valley regions. Modulation of local and systemic immune responses contributes to 2F-MRT treatment efficacy. Furthermore, the double fractionated regimen activates the host immune system, which is mediated, in part, by the circulating cytokines CXCL5, CCL22, and CXCL12. These cytokines are known to stimulate the recruitment of TANs and activated T cells to the primary tumors, as well as influence immune responses against locoregional metastasis (abscopal effect), whose progression was significantly reduced by the second MRT fraction.
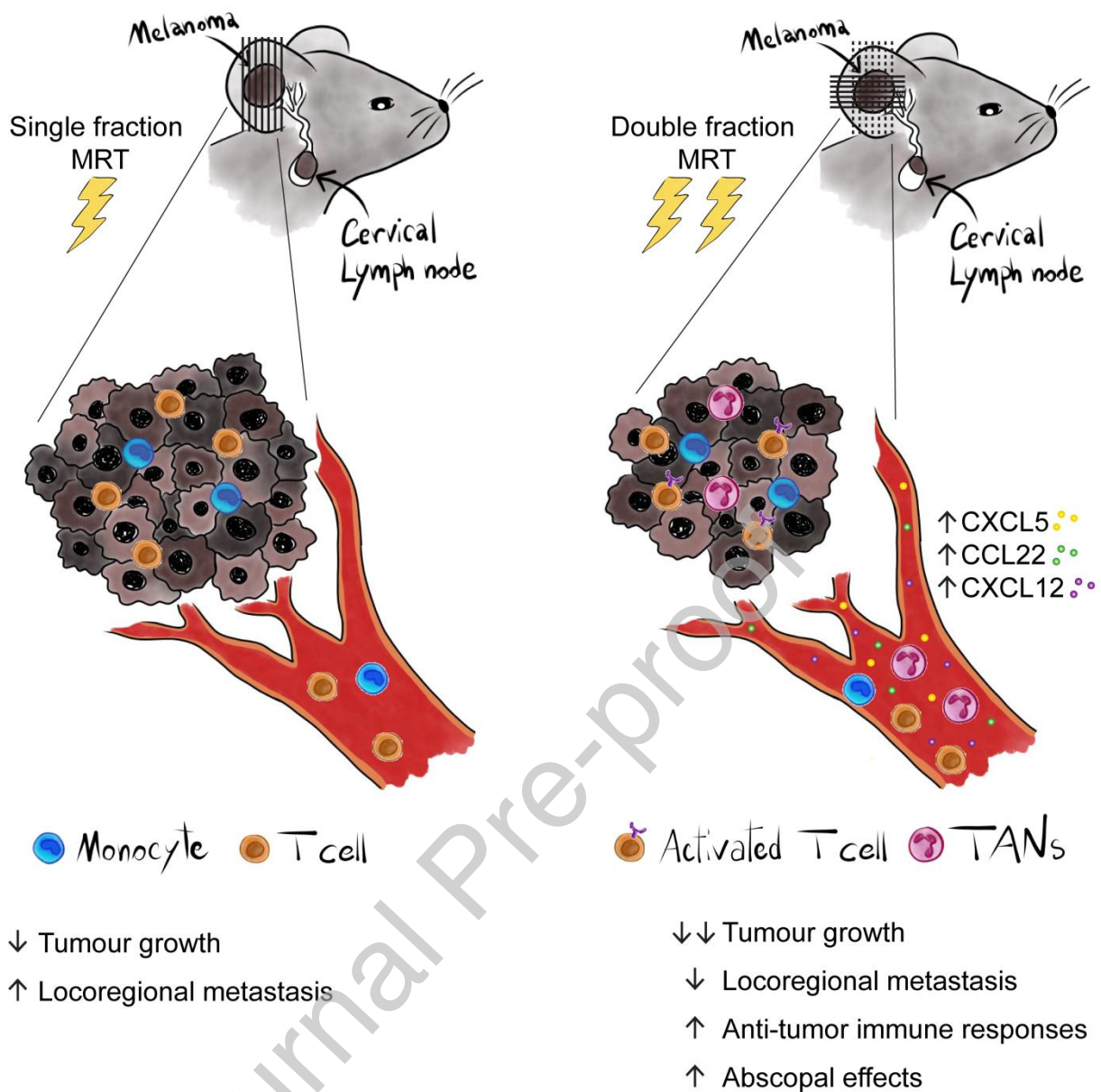
Figure S1. Immunostaining for melanoma marker Melan A and S100β. (A) Positive control (CTR), a primary melanoma tumor. **(B)** LN assigned score 0 contains single melanoma cells infiltrating the LN periphery. Arrows indicate Melan A-positive cells and S100β-positive cells (indicated by arrows). **(C)** LN assigned score 1 show a small group of Melan A/S100β-positive melanoma cells (indicated by arrows) infiltrating the LN periphery. **(D)** For a comparison, absence of melanoma cells in macroscopically negative LNs harvested from a B16F10 melanoma-bearing mouse with a completely ablated tumor by treatment with three 133-Gy MRT daily fractions,

culled at 18 months post-irradiation, is shown (tumor remission). **(E)** Left panel: an example of an excessively large (17.2 mm) LN completely infiltrated by B16F10 melanoma cells, harvested from a mouse with SF-MRT-irradiated tumors at D23 post-irradiation. Right panels: immunostaining of the same LN for Melan A and S100β showing an extensive infiltration by melanoma cells and their tropism to the periphery of the LN and the blood vessels (indicated by arrows).

Figure S2. Metastasis score for individual LNs from CTR, BB, SF-MRT and DF-MRT cohorts and average scores per day. Data shown as an average score per day. Each symbol represents a single LN. LNs in the control group were also scored one day prior to irradiation (D-1). The information on the total number of examined LNs per day is included in **Supplementary Table 1**.

Figure S3. Viability and motility properties of tumor cells in LN metastases and primary melanomas. Microscopic images of histological sections of **(A)** An unusually large LN harvested from a mouse with SF-MRT-irradiated tumors (depictured in Figure S1E, at two different magnifications); **(B)** A primary non-irradiated PFA-fixed melanoma that has been stored in PFA for about 5 years; **(C)** Non-irradiated B16F10 melanoma that has been OCT-frozen at -80ºC after PFA fixation for about 3 years and paraffin-embedded prior to immunostaining **(D)** SF-MRT-irradiated melanoma at D4 post-irradiation, that has been PFA-fixed and OCT-frozen at -80ºC for about 3 years, and paraffin-embedded prior to immunostaining. The sections were immunostained for cleaved caspase-3 (CC3), phospho-histone H3 (PH3), pan-cytokeratin (pan-CK), vimentin, fibronectin and melan A. Only pan-CK, vimentin, fibronectin and melan A immunostaining is reported for panels **(C)** and **(D)**.

41

Note a stronger immunostaining in PFA-fixed-frozen tumors compared to PFA-fixed tumors and a change of the fibronectin immunostaining from nuclei-associated in a non-irradiated tumor to membrane-associated in an MRT-irradiated tumor. Brown, peroxidase immunostaining; blue, nuclei counterstained with hematoxylin; black dots, melanin.

Figure S4. Non-significant changes in plasma concentrations of 19 cytokines in melanoma-bearing mice irradiated with SF-MRT or 2F-MRT. Plasma concentrations of shown cytokines were measured by the multiplex immunoassay in samples of melanoma-bearing animals collected after SF-MRT (pink bars, D2-12) and 2F-MRT (blue bars, D12-22). CCL1 has no data detected for the group SF-MRT D12 and in other 5 groups, N≤3. For CCL5, N=2 for the groups SF-MRT D2, D5 and D9. For CCL2, N=2 for the group 2F-MRT D2. For CC27 and CXCL1, n≤3 for each group and time point. For the rest of the cytokines, N=5 per each time point (with the only exception of MRT D12, n=4). Data shown as a mean concentration ± SD (Kruskal–Wallis non-parametric multiple comparison test).